

Effects of shell correction on α -decay systematicsJing Zhang  and Hong Fei Zhang **School of Nuclear Science and Technology, Lanzhou University, Lanzhou 730000, People's Republic of China*

(Received 6 May 2020; revised 30 June 2020; accepted 17 August 2020; published 7 October 2020)

Within the generalized liquid drop model (GLDM), the effects of the Strutinsky shell correction on α decay processes have been systematically studied. Before the scission point, the shell correction energy E_{sh} , which brings noticeable change to potential barriers for most nuclei, varies with nuclear deformation described by quasimolecular shapes (QMSs). To investigate the subsequent influence on α decay, we performed systematic calculations involving more than 400 favored ground-to-ground α emissions with atomic number $Z = 52$ to 118. We found that the shell correction remarkably reduces the notorious deviation between theoretical and experimental half-lives around the neutron shell closure $N = 126$. It will also shed new light on predicting α -decay half-life of superheavy nuclei.

DOI: [10.1103/PhysRevC.102.044308](https://doi.org/10.1103/PhysRevC.102.044308)**I. INTRODUCTION**

For heavy and superheavy nuclei, the most important decay mode is α radioactivity. In 1911, Geiger and Nuttall presented a simple empirical law to illustrate the relationship between α decay half-lives, T_{α} , and Q values, Q_{α} [1,2]. In 1928, Gamow proposed that α particles would possibly tunnel through the Coulomb barrier [3]. Now we know the simple form of the Geiger-Nuttall law that can be derived from Gamow's theory in which the nuclear Coulomb barrier penetrability plays an important role. Later on, researchers took many other factors into account to refine the theory, like the centrifugal barrier, the proximity force, and the shape evolution of parent nuclei, not only for a reasonable agreement with α -decay experimental data but also for a better understanding of nuclear structures. However, these refinements leave one problem unsolved, namely the evident deviation between theoretical and experimental results near shell closures, especially around the neutron magic number $N = 126$.

It is well known that α decay systematics around $N = 126$ will change abruptly and thus undermine the predictive power of many α -decay theories. For example, the universal decay law, which is derived from the R -matrix theory, as well as many semiclassical approaches show systematic discrepancy from experimental α decay half-lives, $T_{1/2}^{\text{exp}}$, at $N = 126$ [4,5, and references therein]. Numerous attempts have been made to improve the predictive power in this region. One notable example is the semFIS formula [6], which explicitly depends on valence nucleons and can effectively smooth the increased deviations in the neighbor of magic numbers of nucleons [7,8]. Also, the systematic deviations could be minimized by using empirical formulas of preformation factors that change with changing valence nucleon

number [9–11]. The cluster-formation model can give preformation factors that naturally suppress such shell effects, which are determined by the interaction between surface nucleons [12–14]. In short, these successes suggest that the single-particle characteristics of nuclei are the key to the problem.

In the macroscopic-microscopic method, different parts of the total energy are connected with different bulk properties or microscopic structures of nuclei. The shell correction energy is associated with the density of single-particle levels at the Fermi energy [15] and has been proved to be vital for a better explanation of ground-state deformation [16,17], fission [18], and many other phenomena where shell effects dominate. Some α -decay or cluster emission models assume the difference between Q_{α}^{theo} and Q_{α}^{exp} to be the correction energy related to the ground states of parent and daughter nuclei, e.g., the analytical superasymmetric fission model (ASAF) [19] and the generalized liquid drop model (GLDM) [20]. So in these models, a semiempirical shape-dependent shell correction term scaled by $Q_{\alpha}^{\text{theo}} - Q_{\alpha}^{\text{exp}}$ is introduced into one-body barriers. But the obtained results still show large discrepancies from experimental results at $N = 126$. A macroscopic-microscopic model by Poenaru et al. illustrates the effects of microscopic corrections on potential barriers, but still only when using the semFIS formula can the discrepancies of half-lives be effectively reduced [21]. In our previous studies [22,23], the Myers' shell correction formula [16,24] is applied in the GLDM to study the effects of shell correction on α -decay properties. However, the outcome merely shows an increasing trend of T_{α} for most nuclei and others virtually remain the same.

In this work, we incorporate the Strutinsky shell correction method into the GLDM and study its effects on α -decay systematics. Section II briefly revisits the shell correction method, the shape parametrizations as well as the GLDM. The evaluation procedure of T_{α} is slightly modified and thus is discussed in detail. In Sec. III, we compare and analyze

* zhanghongfei@lzu.edu.cn

the results of potential barriers, α preformation factors, and half-lives, where the role of the shell correction is emphasized. Finally, conclusions are summed up in Sec. IV

II. METHOD

A. Shape parametrization

The QMSs (quasimolecular shapes) that reasonably describe one-body shape evolution are given by [25]

$$R(\theta) = \begin{cases} c_1 \sqrt{1 + (1 - s_1^{-2}) \cos^2 \theta}, & 0 \leq \theta < \frac{\pi}{2}, \\ c_2 \sqrt{1 + (1 - s_2^{-2}) \cos^2 \theta}, & \frac{\pi}{2} \leq \theta < \pi. \end{cases} \quad (1)$$

Assuming volume conservation, the two parameters $s_1 = a/c_1$ and $s_2 = a/c_2$ completely define the shape. c_1 and c_2 are the two radial elongations and a is the neck radius. We use $R = (1.28A^{1/3} - 0.76 + 0.8A^{-1/3})$ to determine the sharp radius of spherical nuclei with an atomic number A . For a given decay channel, the ratio $\eta = R_2/R_1$ between the radii of the future fragments allows us to connect s_1 and s_2 through

$$s_2 = \frac{s_1^2}{s_1^2 + (1 - s_1^2)\eta^2} \quad (s_1, s_2 \geq 0, \eta \leq 1).$$

Also, to calculate single particle levels of axially deformed Woods-Saxon potential, we expand Eq. (1) into multipoles:

$$R(\theta) = r(\theta; \beta) = C(\beta)R_0 \left[1 + \sum_{\lambda=\lambda_0}^M \beta_\lambda Y_{\lambda,0}(\cos \theta) \right], \quad (2)$$

where $C(\beta)$ is a scaling factor constrained by volume conservation. R_0 denotes the radius of the spherical nucleus with identical volume. The maximal order $M = 6$. All coefficients constitute the parameter set $\{\beta_i\}$ that replaces the original parameter set $\{s_i\}$ in Eq. (1). Details of the evaluation of these parameters can be found in Ref. [26]. Here we briefly discuss the choice of λ_0 . It has been mentioned that dipole distortion is important for hyperdeformed nuclei with large elongation and necking [27]. So, we choose $\lambda_0 = 1$, which also means that the center of mass is free to move when performing the analytical conversion. The β parametrized shape obtained this way can perfectly match the original QMS. Finally, as was done in Ref. [27], the β parametrized shape will be shifted as a whole to keep its mass center at the coordinate origin.

B. Deformation energy

For a deformed nucleus, the total energy is constructed in a macro-microscopic manner

$$E = E_V + E_S + E_C + E_{\text{Prox}} + E_{\text{sh}} + E_{\text{pair}}. \quad (3)$$

The volume energy E_V , surface energy E_S , Coulomb energy E_C and proximity energy E_{Prox} take the forms adopted in studies of fission, cluster emission, proton radioactivity, and so on [28–31]. The shape-dependent pairing energy is evaluated with the expressions extracted from the finite-range droplet model, and the specific formula is the same as that in Ref. [30,32].

To obtain the shell correction energy E_{sh} , the standard Strutinsky procedure is performed. Single-particle energies

$\{\varepsilon_i\}$ of deformed nuclei are determined using the WSBETA code [33], and the central potential is in axially deformed Woods-Saxon form,

$$V(r) = \frac{V_0}{1 + \exp\left[\frac{r-R(\theta)}{a}\right]}. \quad (4)$$

Here $r - R(\theta)$ represents the distance from certain point r to the nuclear surface in Eq. (2). The diffuseness parameter is denoted by a . V_0 is the depth of the central potential. The spin-orbit potential is also included in single-particle potential. We use the *universal* parametrization set for the potential in Ref. [33]. Then, the single-particle density $g(\varepsilon) = \sum \varepsilon_i \delta(\varepsilon - \varepsilon_i)$ is smoothed by expansion into Gauss-Hermit polynomials up to the sixth order [15,26,34]. The smoothing width $\gamma = 1.2\hbar\omega_0$, $\hbar\omega_0 = 41A^{-1/3}$ MeV is the mean distance between the gross shells. The outcome of the Strutinsky procedure is

$$\delta E_{\text{sh}} = \sum_{i=1}^{N,Z} \varepsilon_i - \int_{-\infty}^{\tilde{\lambda}} \varepsilon \tilde{g}(\varepsilon) d\varepsilon, \quad (5)$$

where the $\tilde{\lambda}$ is the Fermi energy related to smoothed distribution $\tilde{g}(\varepsilon)$. At last, the shell correction energy is

$$E_{\text{sh}} = c \delta E_{\text{sh}}, \quad (6)$$

where c is a non-negative scaling factor that adjusts the division between the macroscopic and microscopic parts [17,23]. In this work c is evaluated as 0.4.

C. Half-life

The half-life against α decay is calculated by $T_{1/2} = \ln 2/\lambda$ in which the decay constant $\lambda = P_0 \nu P$. The assault frequency ν has been taken in a microscopic way [35–37],

$$\nu = \frac{(G + \frac{3}{2})\hbar}{1.2\pi \mu R^2} \quad (7)$$

where the principal quantum number G is obtained by Wildermuth rule as [36,37] $G = 18$ if $N \leq 82$, $G = 20$ if $82 < N \leq 126$, and $G = 22$ in the region $N > 126$.

According to the Wentzel-Kramers-Brillouin (WKB) approximation, the barrier penetrability P is written as

$$-\ln P = -(\ln P_{\text{in}} + \ln P_{\text{out}}) = \int_{S_{\text{in}}}^0 K(s) ds + \int_{R_s}^{R_{\text{out}}} K(r) dr \quad (8)$$

in which $K(x) = \frac{2}{\hbar} \sqrt{2\mu[V(x) - Q]}$. The reduced mass $\mu = A_1 A_2 / A$. Here s denotes either s_1 or s_2 in Eq. (1). r is the mass center distance between the separated spherical fragments [38]. Classical turning points are pinned down by $V(S_{\text{in}}) = V(R_{\text{out}}) = Q$. The scission configuration where $s = 0$ and $r = R_s = R_d + R_\alpha$ divides the total penetrability P into internal and external (or outer) parts, denoted as P_{in} and P_{out} in Eq. (8). Such a division naturally leads to

$$T_{1/2} = \frac{\ln 2}{P_0 P_{\text{in}} \nu P_{\text{out}}}. \quad (9)$$

In Eq. (8), two different integration variables are used for the one-body and two-body stages. The reason is that different

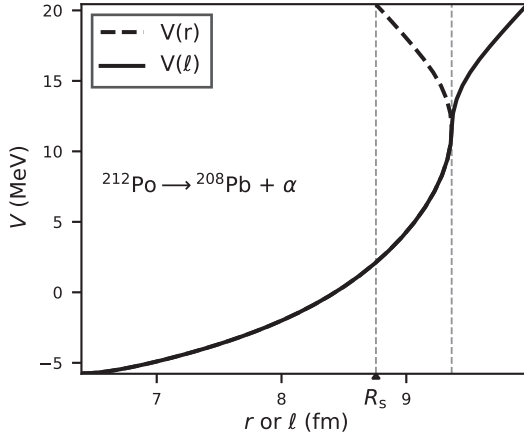


FIG. 1. The liquid drop energy V of ^{212}Po for one-body shapes described by QMS, which includes only E_c , E_s , and E_v for clarity. r and ℓ are two different shape-dependent variables. If the mass asymmetry is large (say in α decay), $V(r)$ will overlap with itself if $r > R_s$. This could be avoided by replacing r with ℓ .

QMSs might correspond to the same mass center distance r . As a result, $V(r)$ will overlap with itself when r exceeds R_s , as shown in Fig. 1. Here we define an alternative variable to r as

$$\ell = \int \left| \frac{dr(s)}{ds} \right| ds, \quad (10)$$

which “unfolds” the overlapping area between the vertical dashed lines and, meanwhile, makes it convenient for us to put the inner and outer barriers together.

III. CALCULATIONS

The shell correction term has an evident impact on deformation barriers, which is illustrated with Fig. 2. If E_{sh} for a spherical nucleus is negative, the nucleus will usually be stable against deformation. For spherical ^{212}Po , the correction energy $E_{\text{sh}}^{\text{sph}} = -3.30\text{MeV}$. So when ^{212}Po is slightly distorted, the deformation energy goes up almost vertically. A ^{212}Po nucleus can decay into a doubly magic ^{208}Pb . The $E_{\text{sh}}^{\text{sph}}$ of ^{208}Pb is -6.32MeV , which will increase potential energy near the scission point. As a result, there is a stronger hindrance effect brought by such negative $E_{\text{sh}}^{\text{sph}}$ via the inner barrier. By contrast, a positive $E_{\text{sh}}^{\text{sph}}$ makes slightly deformed shapes favorable. For example, $E_{\text{sh}}^{\text{sph}} = 5.99\text{MeV}$ for ^{256}Fm and 6.22MeV for ^{252}Cf . In this case, the inner turning point moves forward, which will add to the barrier penetrability. In both cases, the outer barriers remain the same because daughter nuclei are assumed to be spherical. In the following discussion, we will focus on the influences of the Strutinsky shell correction on P_{in} and T_{α} . Systematic calculations are performed for about 400 ground-to-ground α -decay processes with data available in NUBASE2016 [39]. Though an experimental determination of spin and/or parity is lacking for some nuclei, all the relevant α decays are assumed to be favored ones.

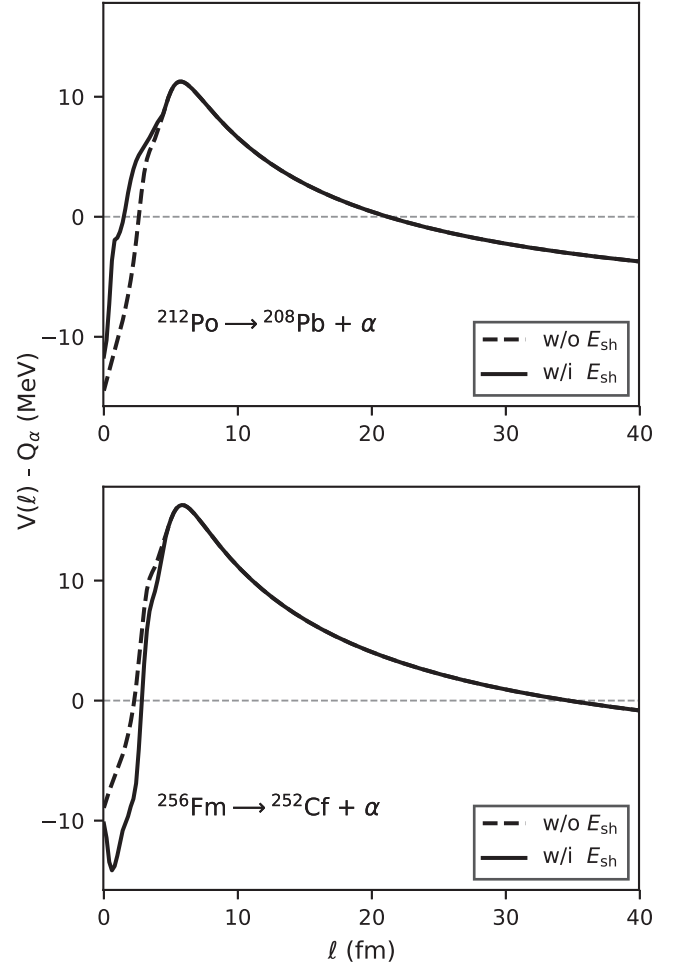


FIG. 2. The alterations of potential barriers for α emitters ^{212}Po and ^{256}Fm .

First, we will analyze the results of preformation factors P_{α} . When the predicted half-life $T_{1/2}^{\text{calc}} = \ln 2 / \nu P_{\text{out}}$, a preformation probability P_{α} would be missing when compared with $T_{1/2}^{\text{exp}}$, which indicates that

$$T_{1/2}^{\text{exp}} = \frac{\ln 2}{P_{\alpha} \nu P_{\text{out}}}. \quad (11)$$

So in the GLDM, P_{α} can be extracted in an empirical way:

$$P_{\text{E}} \equiv \frac{\ln 2}{T_{1/2}^{\text{exp}} \nu P_{\text{out}}}. \quad (12)$$

Its value ranges approximately from 0.1 to 0.01, as shown in Fig. 3(a). The shell effect of P_{E} around $N = 126$ is apparent. Roughly speaking, P_{E} decreases gradually from 0.1 to 0.01 as N approaches 126, but after that it abruptly returns to 0.1. It is worth noting that such an abrupt change of P_{E} across shell closure $N = 126$ might be model independent [40]. In the GLDM, a semiempirical formula has been proposed to reproduce P_{E} and has been frequently used to improve the precision of T_{α} [10,41–43]. For clarity, P_{α} given by the formula

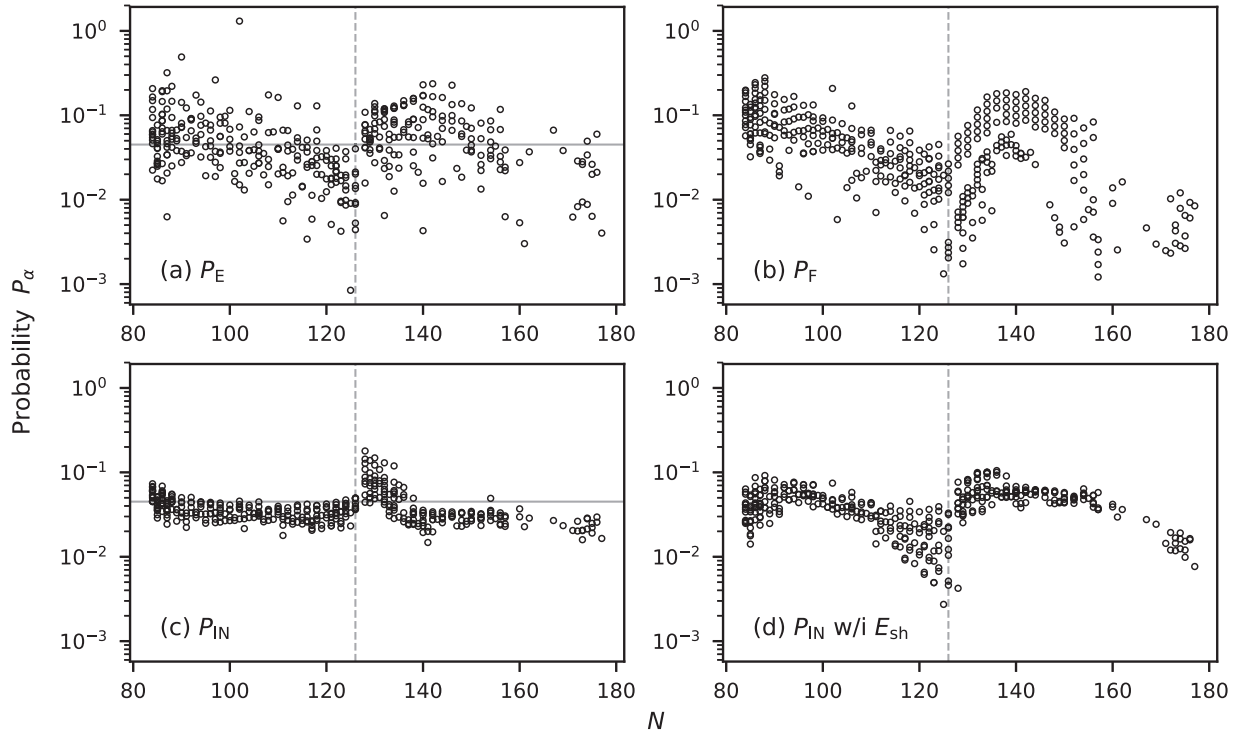


FIG. 3. α preformation probability P_α by different methods (see text for details) versus the neutron number of the emitter, N . Horizontal solid lines in panels (a) and (c) represent $P_\alpha = 0.045$. Vertical dashed lines mark the position of $N = 126$.

is denoted as P_F :

$$P_F \equiv \exp[a + b(Z - Z_1)(Z_2 - Z) + c(N - N_1)(N_2 - N) + dA]. \quad (13)$$

Z_i and N_i are the nearest magic numbers for protons and neutrons. The inclusion of valence nucleon numbers means that the formula contains shell structure information.

Besides, apart from complex formulas, P_E could also be approximated as a global constant. It is sometimes implicitly included in ν [35]. We searched for the optimal value of such a global preformation factor giving the least rms deviation between the constant P_α and the extracted P_E . It turned out to be 0.045, marked by horizontal lines in Fig. 3.

Then, comparing Eqs. (9) and (11), we can find that $P_0 P_{in}$ plays the same role as P_α , which for clarity is denoted by

$$P_{IN} \equiv P_0 P_{in}. \quad (14)$$

Needless to say, P_{IN} and P_{in} will always distribute in a similar pattern since P_0 is simply a positive constant. In the present study $P_0 = 0.22$, evaluated through a fitting procedure where the least rms deviation between P_{IN} without shell correction and P_E is obtained. It might be a coincidence that P_α of ^{212}Po evaluated by the cluster-formation model also equals 0.22 [12,14,44]. In Fig. 3(c), after N crosses 126, P_{IN} will suddenly become several times larger. This is mainly caused by an abrupt increase of Q_α^{exp} . On the whole, P_{IN} is virtually flat, which leads to the fact that P_{IN} without shell correction is close to 0.045.

Here, to introduce shell correction, the scaling factor c in Eq. (6) would be evaluated as 0.4 according to Fig. 4. Just

as how one can obtain the coefficients in Eq. (13) of P_F , the factor c is determined through minimization of a quantity $\sqrt{\sum (\ln P_{IN} - \ln P_E)^2 / n}$ for 414 α emitters. The range of P_{IN} obtained this way, shown in Fig. 3(d), accords well with that of P_E . They are also similar in pattern of distribution. Overall, the theoretical results obtained with shell correction are in good agreement with experimental data.

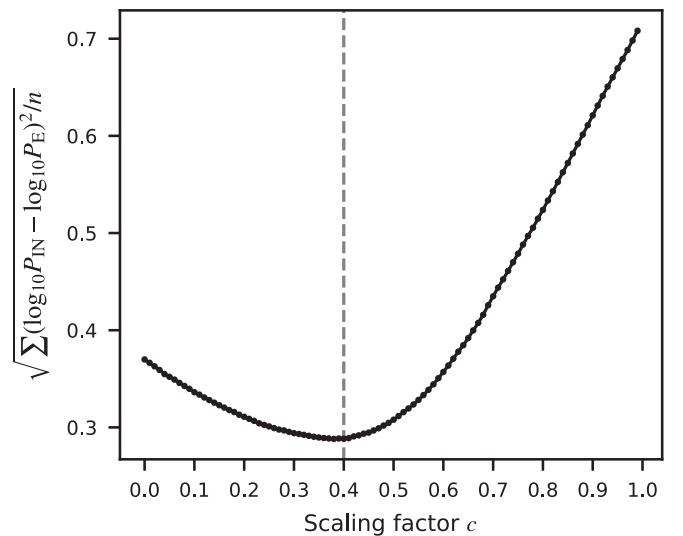


FIG. 4. The optimal value of the scaling factor c is determined as 0.4. These dots on the curve are obtained by varying c from 0 to 1 with a step size of 0.01.

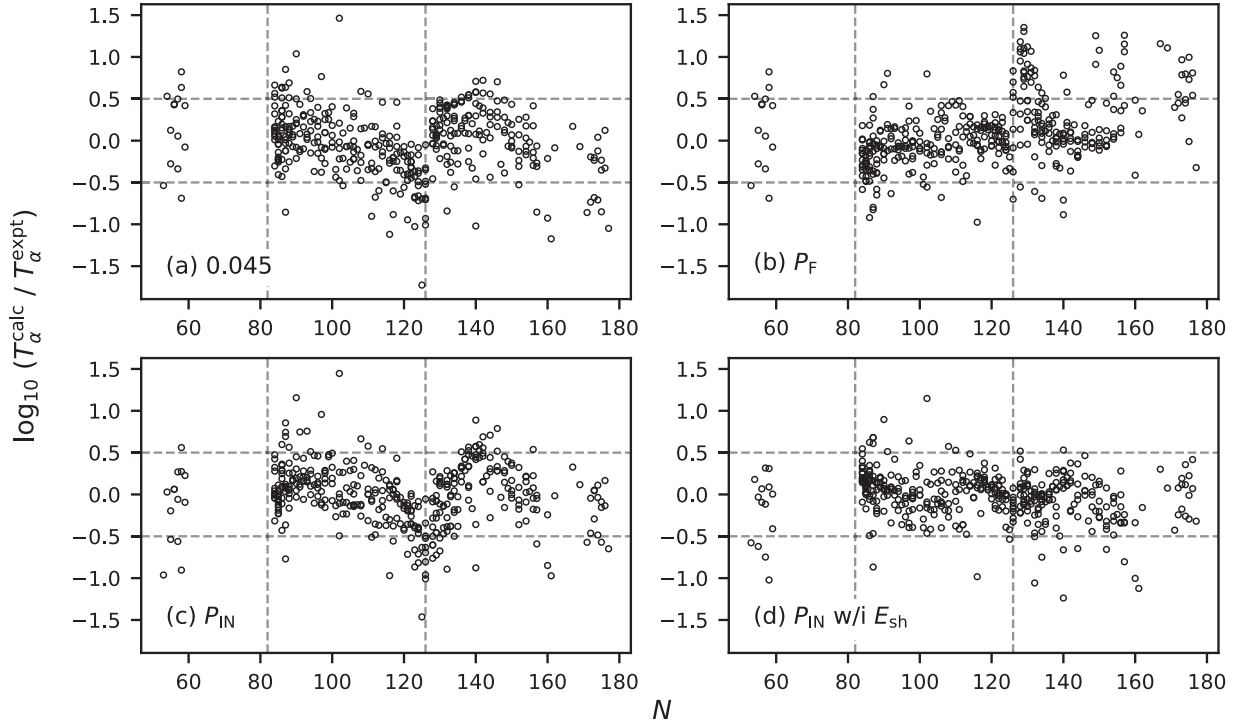


FIG. 5. Deviations between theoretical and experimental T_α on logarithmic scale versus the neutron number, N , of the emitter. The value of P_α used in each panel is annotated. Magic numbers $N = 82$ and 126 are marked by the vertical dashed lines. The upper horizontal dashed line represents $T_\alpha^{\text{calc}}/T_\alpha^{\text{expt}} = 3.16$, while the lower one represents $T_\alpha^{\text{calc}}/T_\alpha^{\text{expt}} = 0.316$. Detailed results can be found in the Supplemental Material [48].

By comparison, P_{IN} with shell correction is obviously closer to P_E . But P_E are still more scattered than P_{IN} in the regions $N \approx 100$ and $N > 130$. One possible explanation is that the daughter nuclei of these emitters should be distorted. For example, the octupole deformation is evident in ground-state shapes at $N = 130$, and so is hexadecapole deformation around $N = 140$ [45]. It has been pointed out that considering the deformation effect can improve the theoretical description of α -decay half-lives [46,47]. We will explore its influence within the GLDM in future studies after finding a way to smoothly connect QMSs of parent nuclei and shapes of distorted fragments, where the orientation of daughter nuclei matters. One thing worth noting is that such deformation effect would not affect our current discussion about α emitters located around magic numbers in Fig. 3 because the relevant nuclei are virtually free of distortion [45].

Having compared different types of preformation factors, we present the results of theoretical half-lives $T_{1/2}^{\text{calc}}$. The deviations between $T_{1/2}^{\text{calc}}$ and $T_{1/2}^{\text{exp}}$ for each of the 414 nuclei are illustrated in Fig. 5. In Fig. 5(b), high precision is achieved by P_F except at $N \approx 130$ and $N > 155$. In addition, Figs. 5(a) and 5(c) are quite similar as expected and both show the largest deviation at $N = 126$. By contrast, the Strutinsky shell correction significantly improves the accuracy of $T_{1/2}^{\text{calc}}$. Most points lie between ± 0.5 in Fig. 5(d), which means $0.316 < T_{1/2}^{\text{calc}}/T_{1/2}^{\text{exp}} < 3.16$. Generally speaking, the inclusion of E_{sh} will increase α decay half-lives around the neutron shell closure at $N = 126$. Hence, for isotopes of $Z = 84-87$

in Fig. 6, the obvious shell effect is diminished. But instead of following a simple upward pattern [22,23], $T_{1/2}^{\text{calc}}$ starts decreasing roughly when $N > 130$ due to a positive E_{sh} . This trend could be clearly observed in the $Z = 90-93$ isotopic chains presented in Fig. 7.

At last, the systematic discrepancy is quantified both by the rms deviation

$$\sigma = \sqrt{\frac{1}{n} \sum (\ln T_{1/2}^{\text{calc}} - \ln T_{1/2}^{\text{exp}})^2}$$

in Table I and by the average absolute deviation

$$\sigma_A = \frac{1}{n} \sum |\ln T_{1/2}^{\text{calc}} - \ln T_{1/2}^{\text{exp}}|$$

in Table II. As is shown, the total average deviation σ_A is instantly reduced by 25.7%. Also, we can adopt a factor $S =$

TABLE I. The rms deviations σ of $T_{1/2}^{\text{calc}}$ from $T_{1/2}^{\text{exp}}$ for different evaluation methods of P_α .

Nuclide	σ			
	$P_\alpha = 0.045$	P_F	P_{IN}	$P_{\text{IN}} \text{ w/i } E_{\text{sh}}$
Even-even (184)	0.372	0.281	0.354	0.254
Doubly odd (52)	0.505	0.506	0.402	0.266
Odd-A (178)	0.372	0.498	0.376	0.326
Total (414)	0.391	0.417	0.370	0.288

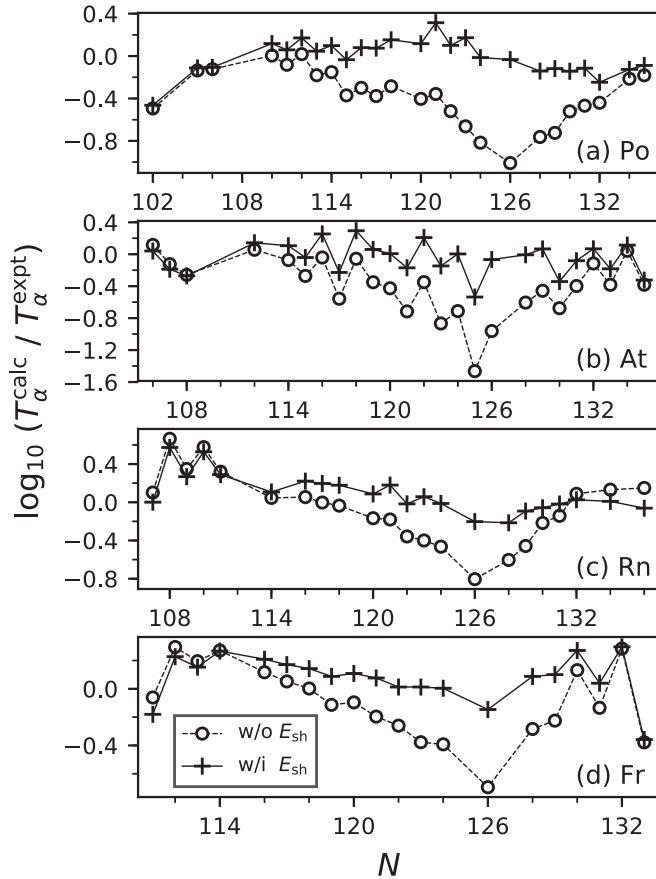


FIG. 6. The same as Fig. 5 but only for $P_\alpha = P_{IN}$ with or without shell correction. Shell effects for isotopes of $Z = 84-87$ are suppressed after introducing E_{sh} .

10^{σ_A} to measure absolute deviations as was done in Ref. [47]. For 184 even-even nuclei, $\sigma_A = 0.188$ and $S \approx 1.54$, which means $T_{1/2}^{calc}$ are statistically within the range 35% smaller to 54% larger than $T_{1/2}^{exp}$. The improvements of σ are similar, which is also reduced by 22%. The average deviations for even-even α emitters obtained with different models are listed in Table III for comparison.

IV. CONCLUSION

The Strutinsky shell correction has been incorporated into the GLDM and significantly improves the accuracy of predicting α -emission half-lives. To obtain the shape-dependent correction energy, we perform an analytical conversion from

TABLE II. The same as Table I but for average deviations σ_A .

Nuclide	σ_A			
	$P_\alpha = 0.045$	P_F	P_{IN}	P_{IN} w/i E_{sh}
Even-even (184)	0.303	0.199	0.275	0.188
Doubly odd (52)	0.369	0.366	0.288	0.200
Odd-A (178)	0.282	0.384	0.283	0.232
Total (414)	0.302	0.300	0.280	0.208

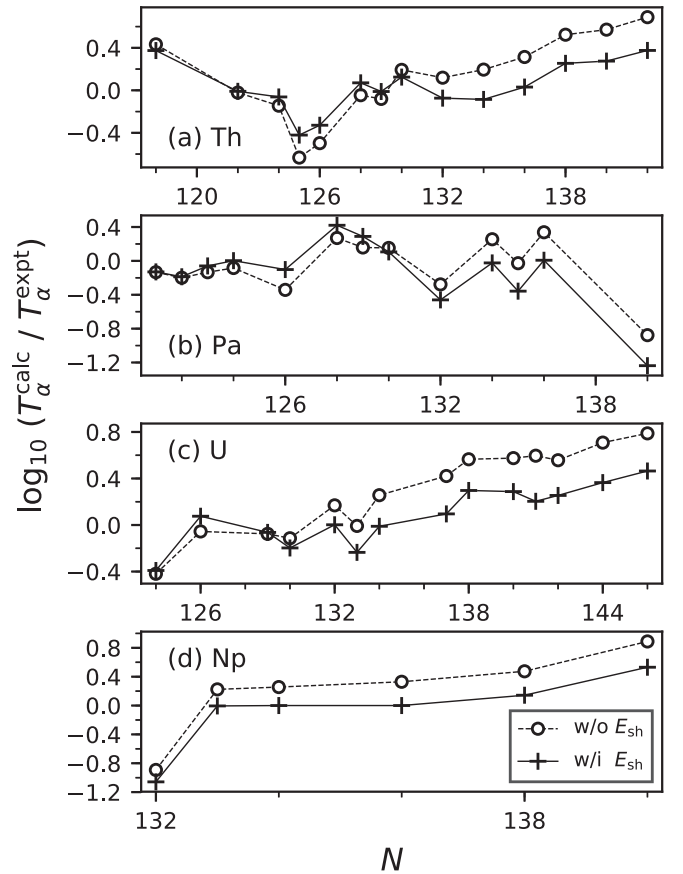


FIG. 7. The same as Fig. 6 but for isotopes of $Z = 90-93$. If E_{sh} is introduced, T_α^{calc} will decrease approximately when N exceeds 130.

asymmetric QMS into β parametrization. Then we perform the standard Strutinsky procedure, which is vital for evaluating the correction energy. After properly evaluating the global scaling factor of shell correction energy, we compare the preformation factors extracted from experimental data and those given by the inner penetrability with shell correction. A similarity between them is manifested. As a consequence, we can effectively reproduce the abrupt change of α decay systematics at $N = 126$. Besides, the effect of shell correction might differ for α emitters with different neutron numbers. While theoretical half-lives around $N = 126$ increase a lot, in regions far from neutron magic numbers (especially when $130 < N < 160$) the half-lives will decrease. Overall, the statistical deviations between the calculated and experimental

TABLE III. Comparison of average deviations of the density-dependent cluster model (DDCM) [46], the dynamic double-folding potential (DDFP) approach [47], the modified Royer's formula (MRF) [49] and this work. Only results of even-even α emitters are listed below.

	DDCM	DDFP	MRF	This work
Number	157	135	137	184
σ_A	0.209	0.210	0.198	0.188

half-lives are minimized by the Strutinsky shell correction. For instance, the average absolute and the rms deviation are reduced by 22% and 26% respectively. In conclusion, the Strutinsky shell correction is indispensable for an accurate description of α decay within the GLDM. In future studies, we should take into account ground-state deformations of daughter nuclei to refine the method, which might further improve the results where such deformation effect is obvious.

ACKNOWLEDGMENTS

This work is supported by the National Natural Science Foundation of China (Grants No. 10775061,

No. 11175054, No. 11675066, No. 11665019, and No. 11947229), by the Fundamental Research Funds for the Central Universities (Grants No. lzujbky-2017-ot04 and No. lzujbky-2020-it01), and by the Feitian Scholar Project of Gansu province.

APPENDIX: SUPPLEMENTAL MATERIAL

Experimental Q values, shell corrections of spherical nuclei, and calculated and experimental half-lives used to produce Fig. 5 can be found in the Supplemental Material [48].

-
- [1] H. Geiger and J. Nuttall, *London Edinburgh Dublin Philos. Mag. J. Sci.* **22**, 613 (1911).
- [2] H. Geiger, *Z. Phys.* **8**, 45 (1922).
- [3] G. Gamow, *Z. Phys.* **51**, 204 (1928).
- [4] O. A. P. Tavares, S. B. Duarte, O. Rodríguez, F. Guzmán, M. Gonçalves, and F. García, *J. Phys. G: Nucl. Part. Phys.* **24**, 1757 (1998).
- [5] C. Qi, A. N. Andreyev, M. Huyse, R. J. Liotta, P. Van Duppen, and R. A. Wyss, *Phys. Rev. C* **81**, 064319 (2010).
- [6] D. N. Poenaru, M. Ivascu, and D. Mazilu, *Comput. Phys. Commun.* **25**, 297 (1982).
- [7] D. N. Poenaru, I.-H. Plonski, and W. Greiner, *Phys. Rev. C* **74**, 014312 (2006).
- [8] D. N. Poenaru, H. Stöcker, and R. A. Gherghescu, *Eur. Phys. J. A* **54**, 14 (2018).
- [9] Y. Hatsukawa, H. Nakahara, and D. C. Hoffman, *Phys. Rev. C* **42**, 674 (1990).
- [10] H. F. Zhang, G. Royer, Y. J. Wang, J. M. Dong, W. Zuo, and J. Q. Li, *Phys. Rev. C* **80**, 057301 (2009).
- [11] W. M. Seif, *J. Phys. G: Nucl. Part. Phys.* **40**, 105102 (2013).
- [12] S. M. Saleh Ahmed, R. Yahaya, S. Radiman, and M. Samudi Yasir, *J. Phys. G: Nucl. Part. Phys.* **40**, 065105 (2013).
- [13] D. Deng, Z. Ren, D. Ni, and Y. Qian, *J. Phys. G: Nucl. Part. Phys.* **42**, 075106 (2015).
- [14] D. Deng and Z. Ren, *Phys. Rev. C* **93**, 044326 (2016).
- [15] V. Strutinsky, *Nucl. Phys. A* **95**, 420 (1967).
- [16] W. D. Myers and W. J. Swiatecki, *Nucl. Phys.* **81**, 1 (1966).
- [17] N. Wang, M. Liu, and X. Wu, *Phys. Rev. C* **81**, 044322 (2010).
- [18] M. Brack, J. Damgaard, A. S. Jensen, H. C. Pauli, V. M. Strutinsky, and C. Y. Wong, *Rev. Mod. Phys.* **44**, 320 (1972).
- [19] D. N. Poenaru, M. Ivascu, and A. Sandulescu, *J. Phys. G: Nucl. Phys.* **5**, L169 (1979).
- [20] G. Royer and R. Moustabchir, *Nucl. Phys. A* **683**, 182 (2001).
- [21] D. N. Poenaru, I. H. Plonski, R. A. Gherghescu, and W. Greiner, *J. Phys. G: Nucl. Part. Phys.* **32**, 1223 (2006).
- [22] J. Zhang, E. De-Jun, and H.-F. Zhang, *Chin. Phys. C* **42**, 094101 (2018).
- [23] Z. Ge, C. Li, J. Li, G. Zhang, B. Li, X. Xu, C. A. T. Sokhna, X. Bao, H. Zhang, Y. S. Tsyganov, *et al.*, *Phys. Rev. C* **98**, 034312 (2018).
- [24] W. D. Myers and W. J. Swiatecki, *Anomalies in Nuclear Masses* (University of California, Berkeley, 1966).
- [25] G. Royer and B. Remaud, *Nucl. Phys. A* **444**, 477 (1985).
- [26] H. Zhang, H. Zhang, J. Li, X. Bao, and N. Ma, *Phys. Rev. C* **90**, 054313 (2014).
- [27] P. Jachimowicz, M. Kowal, and J. Skalski, *Phys. Rev. C* **87**, 044308 (2013).
- [28] J. M. Dong, H. F. Zhang, and G. Royer, *Phys. Rev. C* **79**, 054330 (2009).
- [29] X. J. Bao, H. F. Zhang, B. S. Hu, G. Royer, and J. Q. Li, *J. Phys. G: Nucl. Part. Phys.* **39**, 095103 (2012).
- [30] X. Bao, H. Zhang, G. Royer, and J. Li, *Nucl. Phys. A* **906**, 1 (2013).
- [31] G. Royer, A. Escudie, and B. Sublard, *Phys. Rev. C* **90**, 024607 (2014).
- [32] P. Möller, J. Nix, W. Myers, and W. Swiatecki, *At. Data Nucl. Data Tables* **59**, 185 (1995).
- [33] S. Cwiok, J. Dudek, W. Nazarewicz, J. Skalski, and T. Werner, *Comput. Phys. Commun.* **46**, 379 (1987).
- [34] V. Strutinsky and F. Ivanjuk, *Nucl. Phys. A* **255**, 405 (1975).
- [35] H. F. Zhang, G. Royer, and J. Q. Li, *Phys. Rev. C* **84**, 027303 (2011).
- [36] C. Xu and Z. Ren, *Phys. Rev. C* **69**, 024614 (2004).
- [37] J. C. Pei, F. R. Xu, Z. J. Lin, and E. G. Zhao, *Phys. Rev. C* **76**, 044326 (2007).
- [38] G. Royer, N. Mokus, and J. Jahan, *Phys. Rev. C* **95**, 054610 (2017).
- [39] G. Audi, F. G. Kondev, M. Wang, W. Huang, and S. Naimi, *Chin. Phys. C* **41**, 030001 (2017).
- [40] Y. Qian and Z. Ren, *Sci. China: Phys., Mech. Astron.* **56**, 1520 (2013).
- [41] J. M. Wang, H. F. Zhang, and J. Q. Li, *J. Phys. G: Nucl. Part. Phys.* **40**, 045103 (2013).
- [42] J. M. Wang, H. F. Zhang, and J. Q. Li, *J. Phys. G: Nucl. Part. Phys.* **41**, 075109 (2014).
- [43] X. J. Bao, S. Q. Guo, H. F. Zhang, and J. Q. Li, *Phys. Rev. C* **95**, 034323 (2017).
- [44] D.-M. Deng and Z.-Z. Ren, *Nucl. Sci. Technol.* **27**, 150 (2016).
- [45] P. Möller, A. J. Sierk, T. Ichikawa, and H. Sagawa, *At. Data Nucl. Data Tables* **109-110**, 1 (2016).
- [46] C. Xu and Z. Ren, *Phys. Rev. C* **73**, 041301(R) (2006).
- [47] D. Deng, Z. Ren, and N. Wang, *Phys. Lett. B* **795**, 554 (2019).
- [48] See Supplemental Material at <http://link.aps.org/supplemental/10.1103/PhysRevC.102.044308> for details regarding Fig. 5.
- [49] D. T. Akrawy, H. Hassanabadi, S. Hosseini, and K. Santhosh, *Nucl. Phys. A* **975**, 19 (2018).